Construction of the differential surface admittance operator with an extended Fokas method for electromagnetic scattering at polygonal objects with arbitrary material parameters

Dries Bosman, Martijn Huynen, Daniël De Zutter and Dries Vande Ginste

Quest, IDLab, Department of Information Technology, Ghent University/imec
Technologiepark-Zwijnaarde 126, Ghent, Belgium

Abstract

This article presents a novel method to accurately simulate electromagnetic scattering at homogeneous polygonal cylinders with arbitrary material properties. A single source equivalence approach is invoked, allowing to substitute the background medium for the inner material of the scatterer, provided an equivalent surface current density is introduced. We construct the pertinent differential surface admittance operator by means of the Fokas method, establishing a map between the known Dirichlet boundary values and their unknown Neumann counterparts. However, to allow for lossy materials, we extend the Fokas method to complex wavenumbers. The novel formalism, employing pulse-shaped local basis functions, natively supports combined magnetic and dielectric contrast, accurately captures the skin effect, and is conveniently integrated in traditional boundary integral equation formulations. The correctness and versatility of our technique are verified for various examples by means of analytical validation and through comparison with a Poggio-Miller-Chan-Harrington-Wu-Tsai approach, a volume integral equation method and a commercial solver.

Keywords: Differential surface admittance operator, magnetic materials, lossy materials, boundary integral equations, electromagnetic scattering, Fokas method

1. Introduction

Nowadays, one can no longer imagine a world without information technology utilized in virtually every aspect of modern life. To develop the next generation of technological devices, with ever-increasing operating frequencies, design engineers rely on electromagnetic simulation software to accurately predict the behavior of their product and its capability to cope with the challenges posed by the high-frequency context. Since the scale of these structures is such that full-wave effects cannot be neglected, the numerical tools must rigorously solve Maxwell's equations to capture the relevant electromagnetic aspects. More specifically, the skin effect is a notoriously difficult phenomenon to model precisely, as it causes the fields to crowd near the surface of a (lossy) good conductor and therefore either imposes an unreasonably fine discretization in volumetric schemes, such as the finite element method [1], or induces numerical integration issues for surface-based techniques [2]. Furthermore, novel materials, in particular magnetic materials presenting an elevated contrast (see, e.g., [3]), are also problematic to model and typically require specific preconditioning of the pertinent system matrix [4].

An approach to tackle this category of problems invokes the so-called differential surface admittance (DSA) operator [5], which establishes an exact, global relation between the tangential electric field on the boundary and the equivalent surface current density, incorporating the material properties of the considered structure. Consequently, this procedure creates an equivalent problem, whereby the material forming the object under study is replaced by its surrounding medium and an equivalent surface current density is introduced. As such, in the context of a boundary integral equation (BIE) formulation of electromagnetic (scattering) problems, challenging numerical integration involving the Green's function inside a conductive medium is avoided [2]. In its original formulation [5], the DSA method was only applicable to problems involving infinite circular and rectangular cylinders, without magnetic contrast. Since then, multiple extensions have been conceived: to determine the per-unit-of-length parameters of transmission lines including semiconducting materials [6], to triangular cross-sections [7], to three-dimensional (3-D) cylinders and cuboids [8, 9, 10], and, very recently, to situations including combined dielectric and magnetic contrast [11]. The traditional approach to construct the DSA operator requires

the Dirichlet eigenfunctions of the modeled structure, enforcing a restriction to canonical shapes, while the extension presented in [7] involves specific modifications to avoid a significant Gibbs effect, and requires a composition of multiple triangular parts to model arbitrary polygonal shapes. Several modified schemes, theoretically allowing arbitrary shapes and material properties, have been proposed by Patel *et al.* [12, 13, 14, 15, 16, 17]. However, these realizations again rely on the Green's function inside the conductive medium and one could therefore be confronted with numerical issues, especially in challenging cases comprising highly conductive media in the skin effect regime, or a strong material contrast [18].

The surface current density introduced by the DSA method can be represented as the difference of two (rotated) tangential magnetic fields, in the equivalent and original situation, resp. Therefore, the DSA operator can be considered as the difference of two Dirichlet-to-Neumann (DtN) operators, each one mapping a boundary function (the tangential electric field $e_{\tan}$) to its normal derivative ($-\jmath\omega\mu h_{\tan}$, with $h_{\tan}$ the tangential magnetic field). The original Fokas method [19], or unified transform method, provides an elegant framework to solve this kind of boundary value problem (BVP) for linear partial differential equations (PDEs) such as the Helmholtz equation with a real wavenumber. It produces the required DtN map by solving a set of equations called the *global relation*, projected on an appropriate basis. To this end, the pertinent expressions are evaluated for specific, well-chosen points in the complex Fourier plane, resulting in a 'spectral collocation' method [20]. A thorough discussion of the underlying mathematical foundations can be found in [21]. Here, we propose a novel approach to construct the (discretized) DSA operator based on this formalism, providing an extension to arbitrary convex and concave cross-sections that automatically supports combined dielectric and magnetic contrast. It is important to mention that the original Fokas approach for the Helmholtz equation is restricted to real wavenumbers, while, in this paper, we extend it to *complex* wavenumbers, allowing us to model highly conductive (and thus lossy) media as well. To the best of the authors' knowledge, the proposed extension and application of the Fokas method to electromagnetic scattering problems cannot be found in literature.

Section 2 of this paper details the formulation of the Fokas method for the Helmholtz equation with a complex wavenumber, leading to the aforementioned global relation, to be evaluated in collocation points λ. An appropriate set of collocation points Λ is provided in Section 3, based on the notion of a generalized Fourier transform. With these tools at hand, we proceed to the rigorous treatment of our targeted set of problems and the construction of the discretized DSA operator in Section 4. Various validation and application examples are discussed in Section 5 and, finally, our conclusions are formulated in Section 6.

2. Formulation and extension of the Fokas method for the Helmholtz equation with complex wavenumber

Consider an unknown function $\phi(x, y)$ and a known solution $v(x, y)$ which satisfy the Helmholtz equation in domain $\mathcal{S}$:

$$\nabla^2_{xy}\phi + k^2\phi = 0, \tag{1}$$

$$\nabla^2_{xy}v + k^2 v = 0. \tag{2}$$

In this work, we study lossy materials with wavenumber $k \in \mathbb{C}$, with $k^2 = \omega^2\epsilon\mu$, where $\epsilon = \epsilon_{\mathrm{r}}\epsilon_0$ is the permittivity and $\mu = \mu_{\mathrm{r}}\mu_0$ is the permeability. Note that both ϵ_{r} and μ_{r} can be complex: $\epsilon_{\mathrm{r}} = \epsilon'_{\mathrm{r}} - \jmath\sigma/\omega\epsilon_0$ and $\mu_{\mathrm{r}} = \mu'_{\mathrm{r}} - \jmath\mu''_{\mathrm{r}}$, where the conductivity σ and the parameter μ''_{r} account for the electric and magnetic losses, resp. Invoking Green's second identity, we know that

$$\oint_{\partial\mathcal{S}} \left(\phi\frac{\partial v}{\partial n} - v\frac{\partial\phi}{\partial n}\right) \mathrm{d}c = 0. \tag{3}$$

We introduce the complex variable $z = x + \jmath y$ and its complex conjugate $\tilde{z} = x - \jmath y$. The Laplace operator can then be rewritten as

$$\nabla^2_{xy} = 4\frac{\partial^2}{\partial z\partial\tilde{z}}. \tag{4}$$

A possible solution of (2) in terms of z and $\tilde{z}$ is

$$v = e^{-\frac{\jmath k}{2}(\tilde{z}/\lambda + \lambda z)}, \tag{5}$$

while the following expression, obtained by replacing λ with $-1/\lambda$, also satisfies (2):

$$\breve{v} = e^{\frac{\jmath k}{2}(z/\lambda + \lambda\tilde{z})}. \tag{6}$$

Remark that $\breve{v}$ is not the complex conjugate of v, as both k and λ in (5) and (6) may be a complex number. From now on, we will continue our reasoning with (5) only, for conciseness, as the following steps are entirely analogous for (6) and are obtained by again replacing λ with $-1/\lambda$. One should, however, take the results for both solutions into account in the final expression (17).

For an arbitrary function $f(x, y)$, one can prove that

$$\frac{\partial f}{\partial n}\,\mathrm{d}c = -\jmath\frac{\partial f}{\partial z}\,\mathrm{d}z + \jmath\frac{\partial f}{\partial \tilde{z}}\,\mathrm{d}\tilde{z}\,, \tag{7}$$

which results in

$$\frac{\partial v}{\partial n}\,\mathrm{d}c = \frac{k}{2}v(-\lambda\,\mathrm{d}z + \mathrm{d}\tilde{z}\,/\lambda) \tag{8}$$

for v. This allows to reformulate (3) as

$$\oint_{\partial\mathcal{S}} v\left(\phi\frac{k}{2}(-\lambda\,\mathrm{d}z + \mathrm{d}\tilde{z}\,/\lambda) - \frac{\partial\phi}{\partial n}\,\mathrm{d}c\right) = 0. \tag{9}$$

Here, we restrict $\mathcal{S}$ to a polygonal domain with N corners z_n, $n \in \{0, 1, \ldots, N-1\}$, numbered counterclockwise, where $z_N = z_0$, and introduce the following parameter representation on the side connecting z_n and z_{n+1}:

$$z = \frac{z_n + z_{n+1}}{2} + t\frac{z_{n+1} - z_n}{2} \triangleq m_n + t\,h_n, \qquad t \in [-1, 1]. \tag{10}$$

Remark that $\mathrm{d}c = \sqrt{\mathrm{d}x^2 + \mathrm{d}y^2}$ and $\mathrm{d}z = \mathrm{d}x + \jmath\,\mathrm{d}y$, while $\mathrm{d}c = |h_n|\,\mathrm{d}t$. With this representation, (9) becomes

$$\sum_{n=0}^{N-1} e^{-\jmath M_n}\int_{-1}^{1} e^{-\jmath H_n t}\left(A_n\phi_n - B_n\frac{\partial\phi_n}{\partial n}\right)\mathrm{d}t = 0, \tag{11}$$

where $M_n = k/2\cdot(\tilde{m}_n/\lambda + \lambda m_n)$, $H_n = k/2\cdot\left(\tilde{h}_n/\lambda + \lambda h_n\right)$, $A_n = k/2\cdot\left(\tilde{h}_n/\lambda - \lambda h_n\right)$ and $B_n = |h_n|$.

We wish to find a relationship between the known values of ϕ and the unknown values of $\frac{\partial\phi}{\partial n}$ on $\partial\mathcal{S}$. To this end, we introduce the Legendre polynomials as a set of basis functions and enforce (11) for a set of well-chosen λ-values, with a cardinality significantly higher than the number of unknown expansion coefficients P for $\frac{\partial\phi}{\partial n}$. In the end, this leads to an overdetermined system of equations. Specifically, on side n, we expand ϕ_n as follows:

$$\phi_n = \sum_{p=0}^{P-1} C_p^n P_p(t), \tag{12}$$

with P_p the p-th order Legendre polynomial, normalized such that $P_p(1) = 1$. Invoking the orthogonality relation

$$\int_{-1}^{1} P_p(t)P_m(t)\,\mathrm{d}t = \frac{2}{2p+1}\delta_{pm}, \tag{13}$$

the expansion coefficients of ϕ_n are found to be

$$C_p^n = \frac{2p+1}{2}\int_{-1}^{1}\phi_n(t)P_p(t)\,\mathrm{d}t\,. \tag{14}$$

Similarly, the normal derivative of ϕ_n is represented as

$$\frac{\partial\phi_n}{\partial n} = \sum_{p=0}^{P-1} D_p^n P_p(t), \tag{15}$$

with unknown coefficients D_p^n. The Fourier transform of the Legendre polynomials can be determined analytically, which is a useful and important property in our procedure. We find

$$\int_{-1}^{1} e^{-\jmath\tau t}P_p(t)\,\mathrm{d}t = \frac{\sqrt{2\pi\alpha}}{\alpha}I_{p+1/2}(\alpha), \tag{16}$$

with $\alpha = -\jmath\tau$ and where $I_{p+1/2}$ is the modified Bessel function of the first kind and order $p + 1/2$. This enables us to write an approximate, discretized version of the global relation (11):

$$\sum_{n=0}^{N-1} e^{-\jmath M_n} \frac{\sqrt{2\pi\alpha_n}}{\alpha_n} \sum_{p=0}^{P-1} I_{p+1/2}(\alpha_n) \left(A_n C_p^n - B_n D_p^n\right) = 0, \tag{17}$$

where $\alpha_n = -\jmath H_n$. Although it is not explicitly visible, this expression represents an infinite set of equations depending on the complex parameter λ. By solving the overdetermined system (17) together with its complement corresponding to $\breve{v}$, for a well-chosen collection of these collocation points λ, one finds the expansion coefficients D_p^n for the unknown function $\frac{\partial \phi_n}{\partial n}$ at the boundary of the considered polygonal domain, provided ϕ_n is known.

3. Selection of the complex parameter set $\mathbf{\Lambda}$

In this section, we provide some additional insight underlying the reasoning found in [22], to select an appropriate set of λ-values. We return to (11) and recognize the Fourier-like integrals, similar to those found when determining an angular Fourier series:

$$\int_{-\pi}^{\pi} e^{\jmath m\vartheta} f(\vartheta)\,\mathrm{d}\vartheta = \pi \int_{-1}^{1} e^{\jmath m\pi t} f(t)\,\mathrm{d}t\,, \qquad m \in \mathbb{Z}. \tag{18}$$

We rewrite the sum in (11) as

$$\sum_{n=0}^{N-1} e^{-\jmath M_n} \int_{-1}^{1} e^{-\jmath H_n t} f_n(t)\,\mathrm{d}t = e^{-\jmath M_\nu} \left[\int_{-1}^{1} e^{-\jmath H_\nu t} f_\nu(t)\,\mathrm{d}t + \sum_{n=0, n\neq\nu}^{N-1} e^{-\jmath(M_n - M_\nu)} \int_{-1}^{1} e^{-\jmath H_n t} f_n(t)\,\mathrm{d}t\right] \tag{19}$$

The λ-values associated with side ν are chosen such that the first term in (19) becomes a Fourier integral of the type in (18), which requires

$$H_\nu = k/2 \left(\tilde{h}_\nu/\lambda + \lambda h_\nu\right) = -m\pi, \qquad m \in \{0, 1, 2, \ldots\}, \tag{20}$$

leading to the following values for λ_ν:

$$\lambda_\nu = \frac{-m\pi/k \pm \sqrt{(m\pi/k)^2 - |h_\nu|^2}}{h_\nu}. \tag{21}$$

This particular choice ensures a well-conditioned formulation is obtained [22], as elaborated below. Note that we restricted m to nonnegative values in (20), as the remainder of the Fourier series can be covered by the corresponding expression for $\breve{v}$. We do, however, include $m = 0$, as numerical experiments show that this is required to obtain correct results for this choice of collocation points. To simplify the notation in the following argument, we define

$$\breve{\lambda}_\nu^{\pm} \triangleq -m\pi \pm \sqrt{(m\pi)^2 - k^2|h_\nu|^2}, \tag{22}$$

$$\breve{\lambda}_\nu^{\mp} \triangleq -m\pi \mp \sqrt{(m\pi)^2 - k^2|h_\nu|^2}. \tag{23}$$

The argument of the exponential function in the second term of (19), for $\lambda = \lambda_\nu$, then becomes

$$-\jmath(M_n - M_\nu + H_n t) = -\frac{\jmath k}{2}\left[\frac{\tilde{m}_n - \tilde{m}_\nu + \tilde{h}_n t}{\lambda_\nu} + (m_n - m_\nu + h_n t)\lambda_\nu\right] = -\frac{\jmath}{2}\left(\breve{\lambda}_\nu^{\mp}\frac{\tilde{T}}{\tilde{h}_\nu} + \breve{\lambda}_\nu^{\pm}\frac{T}{h_\nu}\right), \tag{24}$$

with $T = m_n - m_\nu + h_n t$, which we can rewrite as

$$-\jmath(M_n - M_\nu + H_n t) = -\jmath\left|\frac{T}{h_\nu}\right|\left(-m\pi\cos\vartheta \pm \jmath\sqrt{(m\pi)^2 - k^2|h_\nu|^2}\sin\vartheta\right), \qquad \text{with } \vartheta = \arg\left(\frac{T}{h_\nu}\right). \tag{25}$$

First, for lossless materials ($\sigma = 0$ and $\mu_\mathrm{r}'' = 0$), and thus $k \in \mathbb{R}$, the exponential behavior entirely depends on the term $\sin\vartheta$ and rapidly increasing contributions from sides $n \neq \nu$ are avoided by ensuring

$\sin\vartheta \geqslant 0$ and selecting the minus sign in front of the square root. This enforces that $0 \leqslant \vartheta \leqslant \pi$, which can be asserted for convex polygons, as illustrated in Fig. 1 for sides $n = 2$ and $\nu = 3$ of an irregular pentagon. As t varies between -1 and 1, the end point of the vector T moves from z_2 to z_3, while the angle ϑ never becomes larger than π, as long as the polygon remains convex.

Next, for materials with conductive losses ($\sigma > 0$ or $\mu_\mathrm{r}'' > 0$), and hence complex wavenumbers, additional care must be taken. The argument of the square root in (25) now becomes

$$(m\pi)^2 + \omega^2\epsilon_0\mu_0 \left[\left(\frac{\sigma\mu_\mathrm{r}''}{\omega\epsilon_0} - \epsilon_\mathrm{r}'\mu_\mathrm{r}' \right) + \jmath \left(\frac{\sigma\mu_\mathrm{r}'}{\omega\epsilon_0} + \epsilon_\mathrm{r}'\mu_\mathrm{r}'' \right) \right] |h_\nu|^2. \tag{26}$$

Given its positive imaginary part, we can always choose the square root to be located in the first quadrant, yielding a positive real and imaginary part. Consequently, again selecting the minus sign in front of the square root, we obtain an exponentially decreasing behavior and numerical issues are avoided.

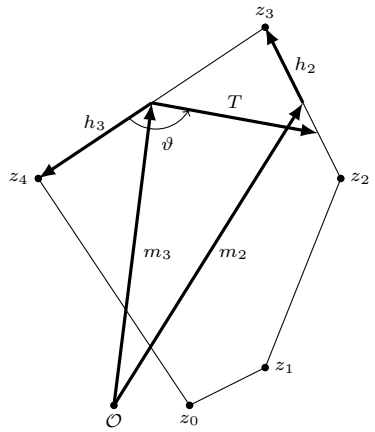

Figure 1: Geometrical interpretation of the restriction to convex polygons.

We exploit these findings to enable the modeling of high magnetic and dielectric contrast in our novel technique and, furthermore, alleviate the restriction to real wavenumbers in the original formulation of the Fokas method. To this end, (17) is modified for each side ν and its corresponding set of λ-values as follows:

$$\sum_{n=0}^{N-1} e^{-\jmath M_n(\lambda_\nu)+\jmath M_\nu(\lambda_\nu)} e^{|\mathbb{R}\mathrm{e}(\alpha_n)|} \frac{\sqrt{2\pi\alpha_n}}{\alpha_n} \sum_{p=0}^{P-1} \breve{I}_{p+1/2}(\alpha_n) \left(A_n(\lambda_\nu) C_p^n - B_n(\lambda_\nu) D_p^n \right) = 0, \tag{27}$$

where $\breve{I}_{p+1/2}$ is the exponentially scaled modified Bessel function of the first kind and $\alpha_n = -\jmath H_n(\lambda_\nu)$. The real part of the argument of the exponential factor is now $\mathbb{R}\mathrm{e}[-\jmath(M_n(\lambda_\nu) - M_\nu(\lambda_\nu) \pm H_n(\lambda_\nu))]$, where the $\pm$-sign originates from the absolute value $|\mathbb{R}\mathrm{e}(\alpha_n)|$. As proven above, this expression remains smaller than or equal to zero for an appropriate choice of λ_ν.

4. Differential surface admittance formalism

Consider transverse magnetic (TM) polarized electromagnetic fields $(\boldsymbol{e}_\mathrm{inc}, \boldsymbol{h}_\mathrm{inc})$, in a time-harmonic regime with $e^{\jmath\omega t}$ dependence, incident on a cylinder with a polygonal cross-section, consisting of an isotropic and homogeneous material with complex permittivity ϵ_i, complex permeability μ_i, and wavenumber k_i. The polygonal domain is denoted by $\mathcal{S}$, with boundary $\partial\mathcal{S}$, outward pointing normal vector $\hat{\boldsymbol{n}}$, and a surrounding medium with constitutive parameters $(\epsilon_\mathrm{e}, \mu_\mathrm{e}, k_\mathrm{e})$, as visualized in Fig. 2a. We adopt a Cartesian coordinate system (x, y, z) and align the longitudinal dimension of the cylinder with the z-axis, implying a z-orientation of the electric fields in our TM problem. As a result of the excitation, scattered fields $(\boldsymbol{e}_\mathrm{sc}, \boldsymbol{h}_\mathrm{sc})$ and fields inside the cylinder $(\boldsymbol{e}_\mathrm{i}, \boldsymbol{h}_\mathrm{i})$ appear.

The differential surface admittance formalism is founded on the single source equivalence theorem, a modified version of Love's theorem [23], without the introduction of a magnetic surface current density, thus accepting arbitrary fields $(\boldsymbol{e}_\mathrm{i}', \boldsymbol{h}_\mathrm{i}')$ inside $\mathcal{S}$. Consequently, the cylinder's inner material may be replaced by its surrounding medium, if an equivalent electric surface current density $\boldsymbol{j}_\mathrm{s}$ is added at the

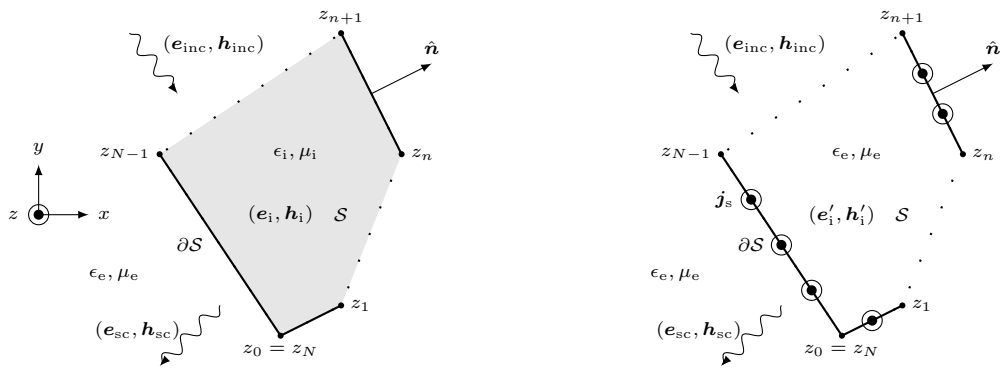

(a) Original problem

(b) Equivalent problem

Figure 2: Illustration of the single source equivalence theorem.

boundary $\partial\mathcal{S}$. The problem at hand is thus modified into the equivalent form of Fig. 2b, allowing us to write that:

$$\boldsymbol{j}_{\text{s}} = \hat{\boldsymbol{n}} \times (\boldsymbol{h}_{\text{i}} - \boldsymbol{h}'_{\text{i}}), \tag{28}$$

$$\hat{\boldsymbol{n}} \times \boldsymbol{e}_{\text{i}} = \hat{\boldsymbol{n}} \times \boldsymbol{e}'_{\text{i}}, \tag{29}$$

at the boundary $\partial\mathcal{S}$. Remark that, since $\boldsymbol{e}_{\text{i}}$ and $\boldsymbol{e}'_{\text{i}}$ are z-oriented in our TM case, we find $\boldsymbol{e}_{\text{i}} = \boldsymbol{e}'_{\text{i}} \triangleq e_z \hat{\boldsymbol{z}}$ on $\partial\mathcal{S}$.

To determine the unknown equivalent surface current density $\boldsymbol{j}_{\text{s}}$, we employ the Dirichlet-to-Neumann operator $\mathcal{X}$, casting the tangential electric field $\boldsymbol{e}$ in any point on $\partial\mathcal{S}$ onto its normal derivative, i.e., the scaled, rotated tangential magnetic field $-\jmath\omega\mu(\hat{\boldsymbol{n}} \times \boldsymbol{h})$. For the original problem Fig. 2a, we obtain

$$-\jmath\omega\mu_{\text{i}}(\hat{\boldsymbol{n}} \times \boldsymbol{h}_{\text{i}}) = \mathcal{X}\boldsymbol{e}, \tag{30}$$

while the situation represented in Fig. 2b results in

$$-\jmath\omega\mu_{\text{e}}(\hat{\boldsymbol{n}} \times \boldsymbol{h}'_{\text{i}}) = \mathcal{X}'\boldsymbol{e}. \tag{31}$$

By taking the difference of (31) and (30), while utilizing (28), we finally obtain the following result for $\boldsymbol{j}_{\text{s}}$:

$$\boldsymbol{j}_{\text{s}} = \hat{\boldsymbol{n}} \times (\boldsymbol{h}_{\text{i}} - \boldsymbol{h}'_{\text{i}}) = -\left(\frac{\mathcal{X}}{\jmath\omega\mu_{\text{i}}} - \frac{\mathcal{X}'}{\jmath\omega\mu_{\text{e}}}\right)\boldsymbol{e} \triangleq \mathcal{Y}\boldsymbol{e}, \tag{32}$$

where $\mathcal{Y}$ is the targeted DSA operator.

Now we expand e_z and $\boldsymbol{j}_{\text{s}} = j_{s,z}\hat{\boldsymbol{z}}$ into a series of Legendre polynomials on each side n, like we did earlier, in Section 2, invoking the parametrization defined in (10):

$$e_z = \sum_{n=0}^{N-1} \sum_{p=0}^{P_n-1} \beta_p^n P_p(t), \tag{33}$$

$$j_{s,z} = \sum_{n=0}^{N-1} \sum_{p=0}^{P_n-1} \iota_p^n P_p(t) \tag{34}$$

By collecting the coefficients β_p^n and ι_p^n into vectors $\boldsymbol{\beta}$ and $\boldsymbol{\iota}$, while stacking the contributions corresponding to the different sides of the polygonal domain, we find the discretized version of (32):

$$\boldsymbol{\iota} = \boldsymbol{\Upsilon}\boldsymbol{\beta}, \tag{35}$$

where the DSA matrix $\boldsymbol{\Upsilon}$ in the domain of the Legendre polynomials is still to be determined. We therefore need to find a map from $\phi = e_z$ to its normal derivative $\frac{\partial\phi}{\partial n} = -\jmath\omega\mu_{\text{i}}h_{\tan}$ and $\frac{\partial\phi}{\partial n} = -\jmath\omega\mu_{\text{e}}h'_{\tan}$ in the original and equivalent situation, respectively, for each individual basis function in the expansion of ϕ. To this end, for both of these situations, the system of equations (27) must be solved $N \times P$ times, with C_p^n equal to zero for all but one tuple $(\check{p}, \check{n})$. Remark that, when solving these overdetermined systems of equations, we rescale each row such that the sum of the absolute values of the row elements

in the system matrix is equal to unity, greatly improving the conditioning. Each iteration results in a column of $\boldsymbol{X}$ or $\boldsymbol{X}'$: a set of coefficients D_p^n, describing the tangential magnetic field corresponding to the contribution by a single Legendre function $\breve{p}$ on side $\breve{n}$. Eventually, we find

$$\boldsymbol{\Upsilon} = \frac{\boldsymbol{X}'}{\jmath\omega\mu_\mathrm{e}} - \frac{\boldsymbol{X}}{\jmath\omega\mu_\mathrm{i}}. \tag{36}$$

To enable a convenient integration of the DSA technique in a traditional BIE framework, we wish to expand e_z and $j_{s,z}$ by means of pulse basis functions b_q^n, defined as

$$b_q^n(t) = \begin{cases} 1, & t_q^n \leqslant t \leqslant t_{q+1}^n \\ 0, & \text{otherwise,} \end{cases} \tag{37}$$

where $-1 = t_0^n < t_1^n < \ldots < t_{Q_n-1}^n < t_{Q_n}^n = 1$ is a partition on the interval of parameter t corresponding to side n, yielding

$$e_z = \sum_{n=0}^{N-1} \sum_{q=0}^{Q_n-1} v_q^n b_q^n(t), \tag{38}$$

$$j_{s,z} = \sum_{n=0}^{N-1} \sum_{q=0}^{Q_n-1} i_q^n b_q^n(t). \tag{39}$$

To obtain the transformation matrix linking the expansions into Legendre polynomials and pulse basis functions, we equate (33) and (38), as they provide the same result, and test both sides with Legendre polynomials $P_{p'}$:

$$\sum_{n=0}^{N-1} \sum_{p=0}^{P_n-1} \beta_p^n \int_{-1}^{1} P_{p'}(t) P_p(t)\,\mathrm{d}t = \sum_{n=0}^{N-1} \sum_{q=0}^{Q_n-1} v_q^n \int_{-1}^{1} P_{p'}(t) b_q^n(t)\,\mathrm{d}t\,, \tag{40}$$

where (13) is employed for the evaluation of the integrals in the left-hand side. The integrals involving pulse basis functions can also be evaluated analytically, e.g., invoking the following property of Legendre polynomials:

$$(2p+1)P_p(t) = \frac{\mathrm{d}}{\mathrm{d}t}\left[P_{p+1}(t) - P_{p-1}(t)\right]. \tag{41}$$

Note that a change of variables from parameter t to the position c along the boundary results in a scaling with factor $|h_n|$ on both sides of (40), which consequently cancels out. In matrix form, the resulting expression is

$$\boldsymbol{D}\boldsymbol{\beta} = \boldsymbol{M}\boldsymbol{v}, \tag{42}$$

where $\boldsymbol{D}$ is a diagonal scaling matrix and matrix $\boldsymbol{M}$ connects both expansions of e_z. Likewise, we know that (34) and (39) both represent the quantity $j_{s,z}$. Testing both sides with a pulse basis function $b_{q'}^{n'}$, we obtain

$$\sum_{n=0}^{N-1} \sum_{p=0}^{P_n-1} \iota_p^n \int_{-1}^{1} b_{q'}^{n'}(t) P_p(t)\,\mathrm{d}t = \sum_{n=0}^{N-1} \sum_{q=0}^{Q_n-1} i_q^n \int_{-1}^{1} b_{q'}^{n'}(t) b_q^n(t)\,\mathrm{d}t\,, \tag{43}$$

represented in matrix form as

$$\boldsymbol{M}^\mathsf{T}\boldsymbol{\iota} = \boldsymbol{G}\boldsymbol{i}, \tag{44}$$

with $\boldsymbol{G}$ a Gram matrix. Combining (36), (42) and (44) finally yields an expression for the DSA matrix $\boldsymbol{Y}$ in the domain of pulse basis functions:

$$\boldsymbol{G}\boldsymbol{i} = \boldsymbol{M}^\mathsf{T}\boldsymbol{\Upsilon}\boldsymbol{D}^{-1}\boldsymbol{M}\boldsymbol{v} \triangleq \boldsymbol{Y}\boldsymbol{v}. \tag{45}$$

Now, we are prepared to return to the solution of our problem in Fig. 2, i.e., to determine the scattered fields $(\boldsymbol{e}_\mathrm{sc}, \boldsymbol{h}_\mathrm{sc})$. In this 2-D TM case, we express the longitudinal electric field induced by the equivalent differential surface current density as follows:

$$e_{z,\mathrm{sc}}(\boldsymbol{r}) = \jmath\omega\mu_\mathrm{e} \int_{\partial\mathcal{S}} G(k_\mathrm{e}|\boldsymbol{r} - \boldsymbol{r}'|) j_{s,z}(\boldsymbol{r}')\,\mathrm{d}c(\boldsymbol{r}')\,, \tag{46}$$

where G is the 2-D Green's function. In a homogeneous medium with wavenumber k_e, we get

$$G(k_\mathrm{e}|\boldsymbol{r}-\boldsymbol{r}'|) = \frac{j}{4}H_0^{(2)}(k_\mathrm{e}|\boldsymbol{r}-\boldsymbol{r}'|), \tag{47}$$

with $H_0^{(2)}$ the zeroth-order Hankel function of the second kind. The total electric field is found by summing the incident and scattered electric fields:

$$e_z = e_{z,\mathrm{inc}} + e_{z,\mathrm{sc}}, \tag{48}$$

which, on the boundary of the cylinder, can be linked to the equivalent differential surface current density by invoking the DSA operator.

We introduce the expressions (38)–(39), and test (48) with the piecewise constant basis functions $b_{q'}^{n'}$, yielding

$$\sum_{n=0}^{N-1}\sum_{q=0}^{Q_n} v_q^n \int_{\partial\mathcal{S}} b_{q'}^{n'}(c) b_q^n(c)\,\mathrm{d}c = \int_{\partial\mathcal{S}} b_{q'}^{n'}(c) e_{z,\mathrm{inc}}(c)\,\mathrm{d}c + \jmath\omega\mu_\mathrm{e}\sum_{n=0}^{N-1}\sum_{q=0}^{Q_n} i_q^n \int_{\partial\mathcal{S}}\int_{\partial\mathcal{S}'} G(k_\mathrm{e}|\boldsymbol{r}-\boldsymbol{r}'|) b_{q'}^{n'}(c) b_q^n(c')\,\mathrm{d}c'\,\mathrm{d}c\,, \tag{49}$$

or the following matrix equation:

$$\boldsymbol{G}\boldsymbol{v} = \boldsymbol{v}_\mathrm{inc} + \jmath\omega\mu_\mathrm{e}\boldsymbol{A}\boldsymbol{i}. \tag{50}$$

Substituting (45) into (50) gives

$$\boldsymbol{G}\boldsymbol{Y}^{-1}\boldsymbol{G}\boldsymbol{i} = \boldsymbol{v}_\mathrm{inc} + \jmath\omega\mu_\mathrm{e}\boldsymbol{A}\boldsymbol{i}, \tag{51}$$

which we solve for the unknown expansion coefficients $\boldsymbol{i}$. The elements of $\boldsymbol{A}$ and $\boldsymbol{v}_\mathrm{inc}$ are determined by evaluating the pertinent integrals numerically, through Gauss-Legendre quadrature, where particular care has been taken to properly treat the occurring singularities [24].

5. Numerical results

First, we investigate the convergence behavior of the DSA matrix in terms of the number of Legendre basis functions involved in its computation. To this end, we consider a rectangle measuring $1.7\lambda_0 \times 0.6\lambda_0$ (where λ_0 is the wavelength in the outside medium), with material parameters $\epsilon_\mathrm{r} = 4$ and $\mu_\mathrm{r} = 1$, discretized by means of a uniform mesh with segments of length $\lambda_0/10$. The relative error of a diagonal matrix element on the bottom side of the rectangle is determined using $P = 700$ collocation points per side, where the value for $L = 350$ Legendre polynomials is taken as a reference. The result is shown in Fig. 3a, together with the trend line $1/L^3$, which is the expected rate of convergence for the Legendre expansion of Neumann boundary values [25]. Similar behavior can be observed for the nondiagonal matrix elements. For situations with magnetic contrast or lossy conductors, there is also convergence, albeit at a slower rate, as illustrated in Figs. 3b and 3c, for the same rectangular cylinder with modified material properties: $\epsilon_\mathrm{r} = 4$ and $\mu_\mathrm{r} = 10$ resp. $\epsilon_\mathrm{r}' = 1$, $\mu_\mathrm{r} = 1$ and $\sigma = 1 \times 10^7$ S/m. The $1/L$ and $1/L^{3/2}$ trend lines are included for reference purposes.

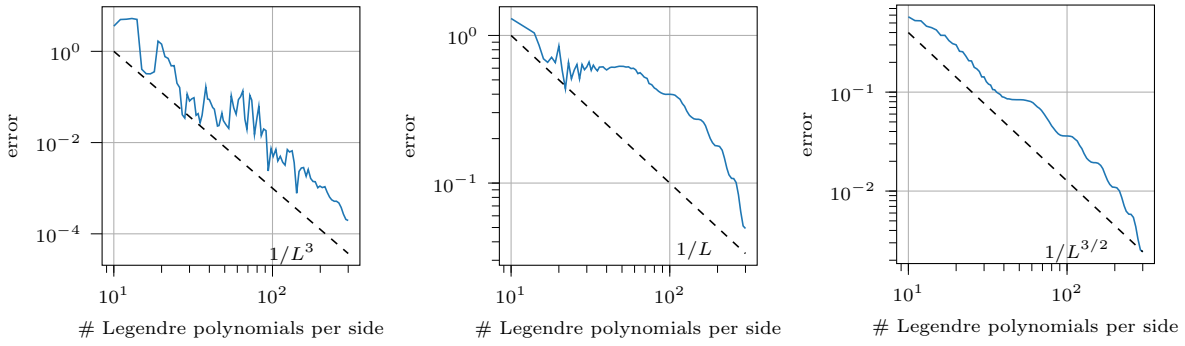

(a) $\epsilon_\mathrm{r} = 4$, $\mu_\mathrm{r} = 1$ (b) $\epsilon_\mathrm{r} = 4$, $\mu_\mathrm{r} = 10$ (c) $\epsilon_\mathrm{r}' = 1$, $\mu_\mathrm{r} = 1$, $\sigma = 1 \times 10^7$ S/m

Figure 3: Relative error of a DSA matrix element as a function of the number of Legendre polynomials per side.

At the corners of a polygonal domain, the electromagnetic fields may exhibit singularities [26], which are not considered explicitly here. In future research, the specific nature of these corner singularities

could therefore be studied and captured more rigorously, e.g., by means of the techniques presented in [25]. In particular, the suggested approach adds global singular functions to the basis, yet this is beyond the scope of the present work.

For a circular cylinder, the 2-D TM scattering of a plane wave can be modeled entirely analytically (see Appendix B of [11]). Therefore, this case serves as a reference to validate our novel method. Consider a circular cylinder with radius 20 cm and material properties $\epsilon'_\mathrm{r} = 3$, $\mu_\mathrm{r} = 8$ and $\sigma \in \{0; 1 \times 10^7\}$ S/m, illuminated by a TM polarized unit plane wave $e_{z,\mathrm{inc}} = e^{-\jmath k_0 \hat{\boldsymbol{u}}_\mathrm{i} \cdot \boldsymbol{r}}$ at a frequency of 1 GHz, incident along $\hat{\boldsymbol{u}}_\mathrm{i} = \hat{\boldsymbol{x}}$. We approximate this structure by means of a cylinder with a regular polygon ($N = 50$) as a cross-section, modeled numerically by means of the DSA-Fokas formalism, with on each side $L = 40$ collocation points, $P = 20$ Legendre polynomials and a uniform partition of $Q = 10$ pulses. These values for the parameters (P, L) will also be utilized in the remaining examples. The tangential electric field at the boundary of both structures is shown in Fig. 4, where a very good agreement is observed. The differences can be fully attributed to the polygonal approximation of the circular cylinder, where the deviation is more prominent in Fig. 4b, corresponding to the $\sigma = 1 \times 10^7$ S/m variant. This was expected, given the nonsmooth boundary and the increase of the fields at the vertices, just as in the case of a conducting wedge [27].

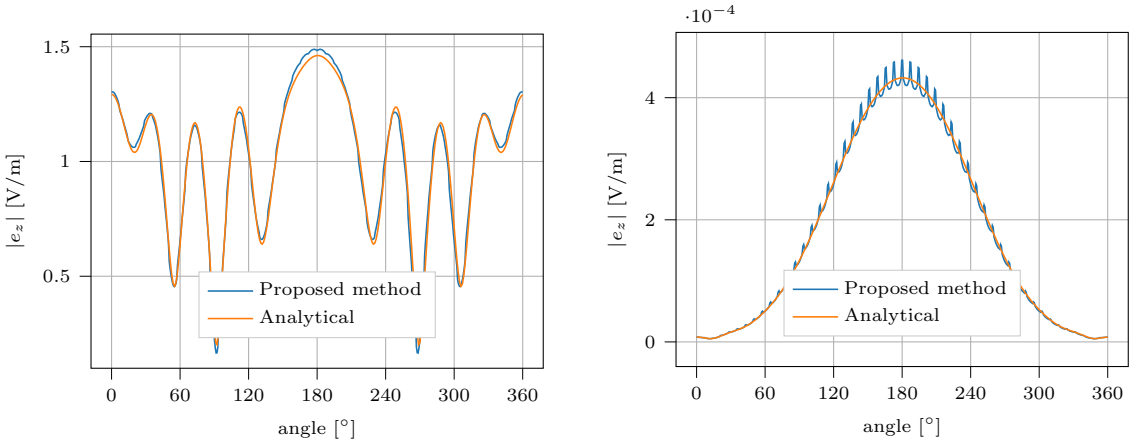

(a) $\sigma = 0$ S/m

(b) $\sigma = 1 \times 10^7$ S/m

Figure 4: Analytically determined magnitude of the tangential electric field at the boundary of a circular cylinder with radius 20 cm and material properties $\epsilon'_\mathrm{r} = 3$, $\mu_\mathrm{r} = 8$ and $\sigma \in \{0; 1 \times 10^7\}$ S/m, at a frequency of 1 GHz, and the numerically calculated result for its polygonal approximation with $N = 50$ sides.

As a second example, we study the echo width or backscattering cross-section of two different rectangular cylinders, excited by a TM polarized plane wave, in Fig. 5, for two methods: the proposed technique and a volume integral equation (VIE) approach [28], serving as an additional validation. For a unit amplitude incident plane wave propagating along $\hat{\boldsymbol{u}}_\mathrm{i}$, the echo width is defined as

$$\sigma(-\hat{\boldsymbol{u}}_\mathrm{i}, \hat{\boldsymbol{u}}_\mathrm{i}) = 2\pi |F(\phi)|^2 \tag{52}$$

with ϕ the angle between the x-axis and $-\hat{\boldsymbol{u}}_\mathrm{i}$, and $F(\phi)$ the far field pattern, given by

$$F(\phi) = -\frac{\omega \mu_\mathrm{e}}{4} \sqrt{\frac{2\jmath}{\pi k_\mathrm{e}}} \int_c e^{\jmath k_\mathrm{e} \hat{\boldsymbol{u}}_\mathrm{i} \cdot \boldsymbol{r}'} j_{s,z}(\boldsymbol{r}') \mathrm{d}c. \tag{53}$$

A normalization with respect to the wavelength λ_0 in the outside medium is applied on the results in Fig. 5, plotted on a dB scale. The first rectangular cylinder has dimensions $1.7\lambda_0 \times 0.6\lambda_0$ and material properties $\epsilon_\mathrm{r} = 1.9 - 1.2\jmath$, $\mu_\mathrm{r} = 3.2 - 0.4\jmath$. The horizontal and vertical sides of the rectangle are subdivided in 170 and 60 segments, resp. Its echo width is shown in Fig. 5a. For the result in Fig. 5b, a $2.3\lambda_0 \times 0.1\lambda_0$ rectangular cylinder with relative permittivity $\epsilon_\mathrm{r} = 2 - 0.5\jmath$ and relative permeability $\mu_\mathrm{r} = 4.5 - 2.5\jmath$ was modeled. Only the discretization was modified with respect to to the former example: 345 and 15 segments are now used on the horizontal and vertical sides, resp. A good agreement between our novel formalism and the VIE reference solution is achieved for both cases.

Next, we consider two polygonal cylinders, to determine the tangential electric field on the boundary and the radar cross-section (RCS), defined as $\sigma(\hat{\boldsymbol{u}}, \hat{\boldsymbol{u}}_\mathrm{i})$, where ϕ in (52) is now the angle between the x-axis and the direction of observation $\hat{\boldsymbol{u}}$.

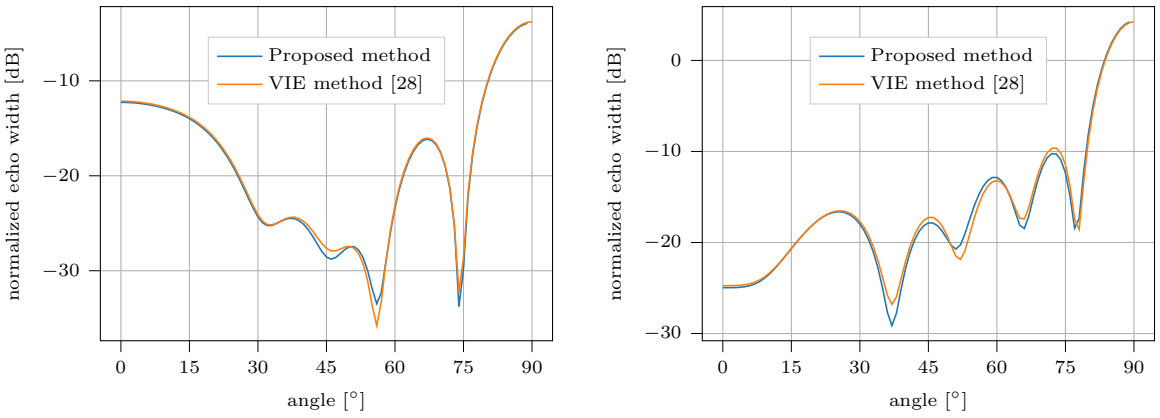

(a) $1.7\lambda_0 \times 0.6\lambda_0$, $\epsilon_\mathrm{r} = 1.9 - 1.2\jmath$, $\mu_\mathrm{r} = 3.2 - 0.4\jmath$

(b) $2.3\lambda_0 \times 0.1\lambda_0$, $\epsilon_\mathrm{r} = 2 - 0.5\jmath$, $\mu_\mathrm{r} = 4.5 - 2.5\jmath$

Figure 5: Echo width, normalized with respect to the wavelength λ_0, of two rectangular cylinders illuminated by a TM polarized plane wave. The reference solutions are found by means of a VIE method [28].

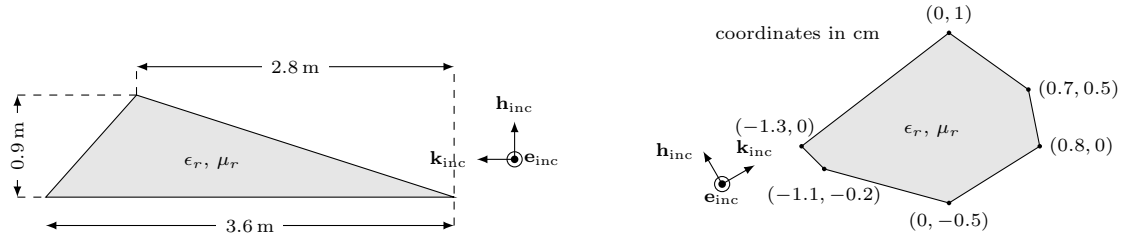

(a) $\epsilon_\mathrm{r} = 3$, $\mu_\mathrm{r} = 7$

(b) $\epsilon'_\mathrm{r} = 1$, $\mu_\mathrm{r} = 5$, $\sigma \in \{1, 10, 100, 1000\}\,\mathrm{S/m}$

Figure 6: Schematic representation of a triangular and a hexagonal cylinder.

In Fig. 6a, we show a schematic representation of a triangular cylinder with material properties $\epsilon_\mathrm{r} = 3$ and $\mu_\mathrm{r} = 7$, excited with a TM polarized plane wave at a frequency of 100 MHz, incident along the negative x-axis. An alternative, competing boundary integral technique, based on the Poggio-Miller-Chan-Harrington-Wu-Tsai (PMCHWT) method [29], and CST Studio Suite [30] serve as a reference to validate our results. The boundary of the triangle is traversed in counterclockwise direction, starting at the bottom left corner. The sides are subdivided uniformly into 252, 206 and 84 segments, resp., each supporting a pulse basis function. For both the tangential electric field and the RCS, our proposed method and the reference solution are in close agreement, as can be observed in Fig. 7.

The hexagonal cylinder of Fig. 6b has material properties $\epsilon'_\mathrm{r} = 1$, $\mu_\mathrm{r} = 5$ and $\sigma \in \{1, 10, 100, 1000\}\,\mathrm{S/m}$. It is illuminated by a TM polarized plane wave at a frequency of 10 GHz, incident under a fixed angle of 30° with the x-axis. With a uniform discretization in segments of approximate length 200 µm (amounting to 268 in total), we obtain the results presented in Fig. 8, for the tangential electric field and the RCS. Once again our novel method and the PMCHWT-based approach correspond very well. Note that for $\sigma = 1000\,\mathrm{S/m}$ the skin depth is 71.2 µm and, hence, the skin effect is well developed.

Finally, we investigate an example with a nonconvex structure, invoking the procedure outlined in [20]. There, 'virtual sides' are introduced, subdividing the nonconvex polygon into convex components. Including the contributions for these virtual sides results in a problem formulation that is mathematically equivalent, but greatly improves the conditioning of the numerical implementation. Referring back to our reasoning in Section 3, we must, however, tolerate a restriction to situations with moderate contrast in this case, to avoid the occurrence of exponentially increasing terms. The shape of the considered object's cross-section is a five-pointed star with inner radius $r = 0.5\,\mathrm{m}$ and outer radius $R = 2\,\mathrm{m}$, as illustrated in Fig. 10. It has material properties $\epsilon_\mathrm{r} = 8$, $\mu_\mathrm{r} = 3$ and is excited by a TM polarized plane wave at a frequency of 100 MHz, incident along the x-axis. Each side of the star shape is subdivided uniformly into 70 segments (amounting to 700 segments in total). The electric field and RCS results for our novel method and the PMCHWT-based reference solution are compared in Fig. 10, demonstrating a very close correspondence.

To conclude this section, we present the CPU time required to determine the DSA matrix by means of a Python implementation of our proposed formalism, in Table 1, for all of the above examples, including

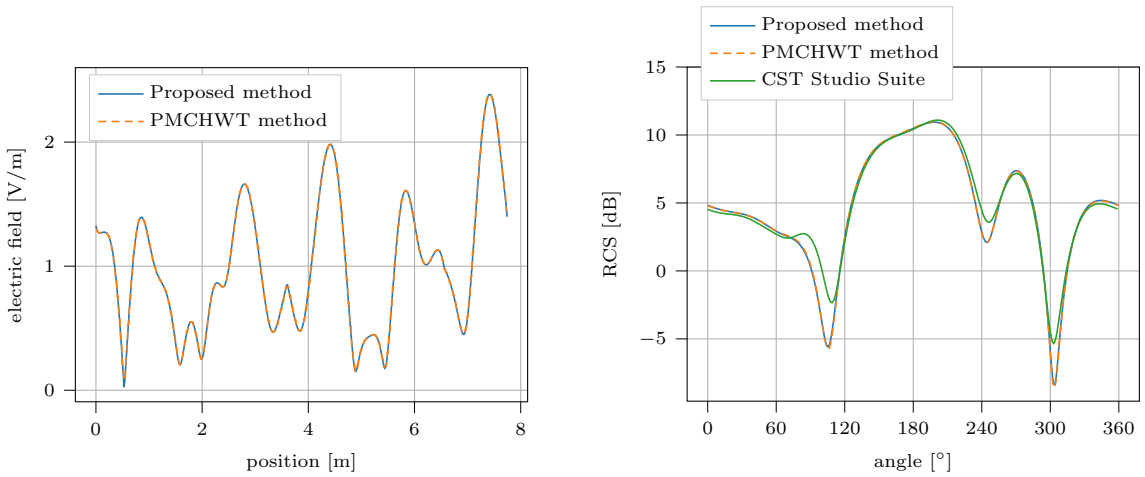

(a) (b)

Figure 7: Magnitude of the tangential electric field on the boundary and radar cross-section of a triangular cylinder (Fig. 6a) with material properties $\epsilon_r = 3$ and $\mu_r = 7$, illuminated by a TM polarized plane wave at a frequency of 100 MHz, incident along the negative x-direction. The reference solutions are obtained by means of a PMCHWT method and CST Studio Suite.

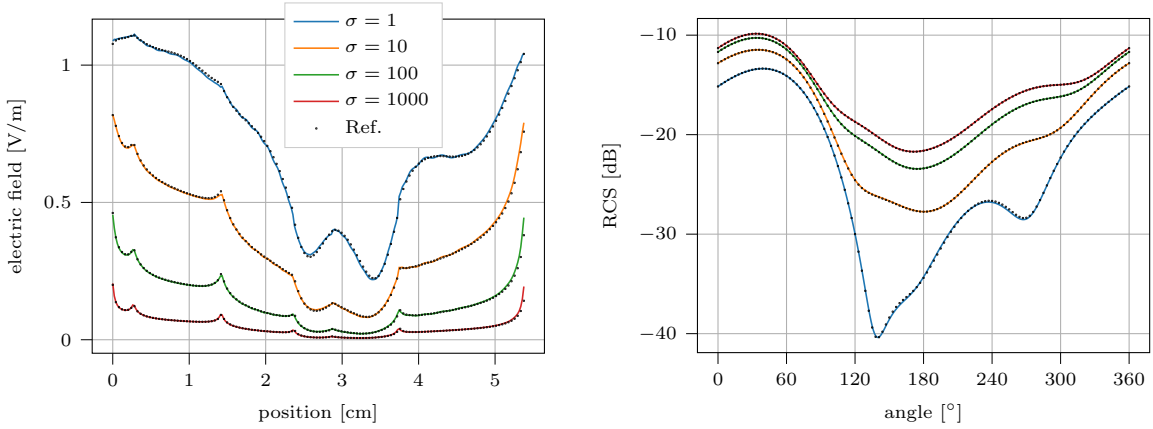

(a) (b)

Figure 8: Magnitude of the tangential electric field on the boundary and radar cross-section of a hexagonal cylinder (Fig. 6b) with material properties $\epsilon_r' = 1$, $\mu_r = 5$ and $\sigma \in \{1, 10, 100, 1000\}$ S/m, illuminated by a TM polarized plane wave at a frequency of 10 GHz, incident under an angle of 30° with the x-axis. The reference solutions are obtained by means of a PMCHWT method.

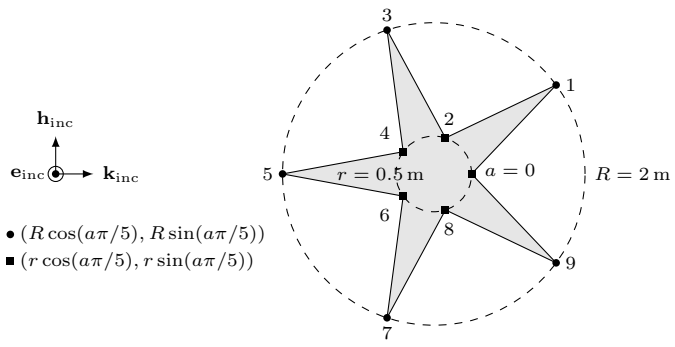

Figure 9: Schematic representation of a cylinder with a regular five-pointed star cross-section.

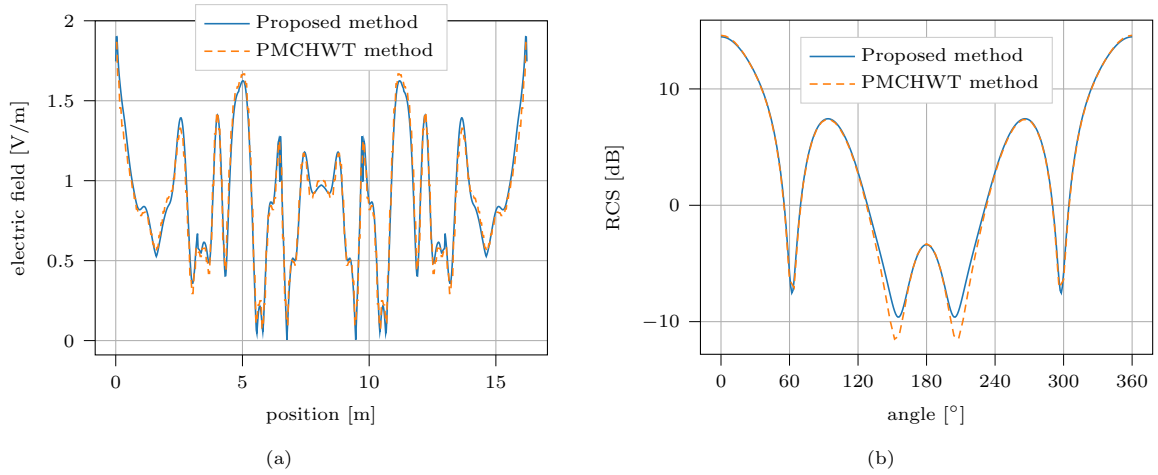

(a) (b)

Figure 10: Magnitude of the tangential electric field on the boundary and radar cross-section of a cylinder with a five-pointed star cross-section (Fig. 9) with material properties $\epsilon_r = 8$ and $\mu_r = 3$, illuminated by a TM polarized plane wave at a frequency of 100 MHz, incident along the x-direction. The reference solutions are obtained by means of a PMCHWT method.

the number of sides and the number of edges in the discretization. This demonstrates the limited computational requirements of our method, in particular when compared to those of the overall BIE framework.

Example	*# sides*	*# edges*	*CPU time [s]*
Fig. 4	50	500	50.6
Fig. 5a	4	460	0.22
Fig. 5b	4	720	0.23
Fig. 7	3	542	0.22
Fig. 8	6	268	0.37
Fig. 10	10	700	2.04

Table 1: CPU timings for the determination of the DSA matrix for all example structures studied in this section.

6. Conclusion

In this work, a novel formulation of the 2-D differential surface admittance (DSA) operator, using the Fokas method, was developed and applied to electromagnetic scattering problems involving cylinders with a polygonal cross-section. We demonstrated how this method can be extended to the important case of general, complex wavenumbers and devoted specific attention to the selection of the collocation points to solve the pertinent global relation. This way, the discretized DSA operator was first determined in the domain of Legendre polynomials and later transformed to a more convenient form with piecewise constant basis functions. Numerous numerical results illustrated the accuracy and versatility of our technique and it was shown that the construction of the DSA operator is computationally efficient.

To further enhance the proposed method, one could, in principle, consider the construction of the DSA matrix for unbounded domains, although this would require additional research to correctly establish the integration in the traditional boundary integral equation framework to solve the type of problems presented in this work. Moreover, in this situation, the proper construction of the global relation and selection of the collocation points become even more crucial due to additional restrictions imposed by the considered (semi-)infinite solution space, as illustrated in [31, 32]. Furthermore, an extension of the Fokas method to curvilinear boundaries has been proposed in [33] and might also be applied in the context of electromagnetic scattering, modeled with the DSA formalism.

References

[1] P. P. Silvester, R. L. Ferrari, Finite elements for electrical engineers, Cambridge University Press, Cambridge, 1996. doi:10.1017/CBO9781139170611.

[2] J. Peeters, I. Bogaert, D. De Zutter, Calculation of MoM interaction integrals in highly conductive media, IEEE Transactions on Antennas and Propagation 60 (2) (2012) 930–940. doi:10.1109/TAP.2011.2173105.

[3] S. Muroga, Y. Endo, M. Tanaka, Inductance evaluation of CPW with Co-Zr-Nb film using magnetic circuit analysis, Journal of Electronic Materials 48 (3) (2019) 1342–1346. doi:10.1007/s11664-018-6835-z.

[4] M. Gossye, D. Vande Ginste, H. Rogier, Electromagnetic modeling of high magnetic contrast media using Calderón preconditioning, Computers and Mathematics with Applications 77 (6) (2019) 1626–1638. doi:10.1016/j.camwa.2018.08.045.

[5] D. De Zutter, L. Knockaert, Skin effect modeling based on a differential surface admittance operator, IEEE Transactions on Microwave Theory and Techniques 53 (8) (2005) 2526–2538. doi:10.1109/TMTT.2005.852766.

[6] T. Demeester, D. De Zutter, Quasi-TM transmission line parameters of coupled lossy lines based on the Dirichlet to Neumann boundary operator, IEEE Transactions on Microwave Theory and Techniques 56 (7) (2008) 1649–1660. doi:10.1109/TMTT.2008.925215.

[7] T. Demeester, D. De Zutter, Construction of the Dirichlet to Neumann boundary operator for triangles and applications in the analysis of polygonal conductors, IEEE Transactions on Microwave Theory and Techniques 58 (1) (2010) 116–127. doi:10.1109/TMTT.2009.2035881.

[8] M. Huynen, M. Gossye, D. De Zutter, D. Vande Ginste, A 3-D differential surface admittance operator for lossy dipole antenna analysis, IEEE Antennas and Wireless Propagation Letters 16 (2017) 1052–1055. doi:10.1109/LAWP.2016.2619558.

[9] M. Huynen, D. De Zutter, D. Vande Ginste, Rigorous full-wave resistance and inductance computation of 3-D interconnects, IEEE Microwave and Wireless Components Letters 28 (6) (2018) 455–457. doi:10.1109/LMWC.2018.2825652.

[10] M. Huynen, K. Y. Kapusuz, X. Sun, G. Van der Plas, E. Beyne, D. De Zutter, D. Vande Ginste, Entire domain basis function expansion of the differential surface admittance for efficient broadband characterization of lossy interconnects, IEEE Transactions on Microwave Theory and Techniques 68 (4) (2020) 1217–1233. doi:10.1109/TMTT.2019.2957485.

[11] D. Bosman, M. Huynen, D. De Zutter, H. Rogier, D. Vande Ginste, A 2-D differential surface admittance operator for combined magnetic and dielectric contrast, Computers and Mathematics with Applications 102 (2021) 175–186. doi:10.1016/j.camwa.2021.10.011.

[12] U. R. Patel, B. Gustavsen, P. Triverio, An equivalent surface current approach for the computation of the series impedance of power cables with inclusion of skin and proximity effects, IEEE Transactions on Power Delivery 28 (4) (2013) 2474–2482. doi:10.1109/TPWRD.2013.2267098.

[13] U. R. Patel, B. Gustavsen, P. Triverio, Proximity-aware calculation of cable series impedance for systems of solid and hollow conductors, IEEE Transactions on Power Delivery 29 (5) (2014) 2101–2109. doi:10.1109/TPWRD.2014.2330994.

[14] U. R. Patel, P. Triverio, MoM-SO: A complete method for computing the impedance of cable systems including skin, proximity, and ground return effects, IEEE Transactions on Power Delivery 30 (5) (2015) 2110–2118. doi:10.1109/TPWRD.2014.2378594.

[15] U. R. Patel, P. Triverio, Skin effect modeling in conductors of arbitrary shape through a surface admittance operator and the contour integral method, IEEE Transactions on Microwave Theory and Techniques 64 (9) (2016) 2708–2717. doi:10.1109/TMTT.2016.2593721.

[16] U. R. Patel, P. Triverio, Accurate impedance calculation for underground and submarine power cables using MoM-SO and a multilayer ground model, IEEE Transactions on Power Delivery 31 (3) (2016) 1233–1241. doi:10.1109/TPWRD.2015.2469599.

[17] U. R. Patel, P. Triverio, S. V. Hum, A novel single-source surface integral method to compute scattering from dielectric objects, IEEE Antennas and Wireless Propagation Letters 16 (2017) 1715–1718. doi:10.1109/LAWP.2017.2669183.

[18] P. Ylä-Oijala, S. P. Kiminki, Challenges in developing efficient Calderón preconditioners for resonating or high material contrast penetrable objects, Journal of Computational and Applied Mathematics 289 (2015) 296–305. doi:10.1016/j.cam.2015.01.005.

[19] A. S. Fokas, A unified transform method for solving linear and certain nonlinear PDEs, Proceedings of the Royal Society A 453 (1962) (1997) 1411–1443. doi:10.1098/rspa.1997.0077.

[20] M. J. Colbrook, N. Flyer, B. Fornberg, On the Fokas method for the solution of elliptic problems in both convex and non-convex polygonal domains, Journal of Computational Physics 374 (2018) 996–1016. doi:10.1016/j.jcp.2018.08.005.

[21] A. C. L. Ashton, On the rigorous foundations of the Fokas method for linear elliptic partial differential equations, Proceedings of the Royal Society A 468 (2141) (2012) 1325–1331. doi:10.1098/rspa.2011.0478.

[22] A. S. Fokas, N. Flyer, S. A. Smitheman, E. A. Spence, A semi-analytical numerical method for solving evolution and elliptic partial differential equations, Journal of Computational and Applied Mathematics 227 (1) (2009) 59–74. doi:10.1016/j.cam.2008.07.036.

[23] C. Balanis, Advanced Engineering Electromagnetics, 2nd Edition, John Wiley & Sons, New Jersey, 2012, Ch. 7, pp. 328–331.

[24] M. S. Tong, W. C. Chew, The Nyström Method in Electromagnetics, John Wiley & Sons, Singapore, 2020.

[25] M. J. Colbrook, T. S. Fokas, P. Hashemzadeh, A hybrid analytical-numerical technique for elliptic PDEs, SIAM Journal on Scientific Computing 41 (2) (2019) A1066–A1090. doi:10.1137/18M1217309.

[26] J. Meixner, The behavior of electromagnetic fields at edges, IEEE Transactions on Antennas and Propagation 20 (4) (1972) 442–446. doi:10.1109/TAP.1972.1140243.

[27] T. Demeester, D. De Zutter, Fields at a finite conducting wedge and applications in interconnect modeling, IEEE Transactions on Microwave Theory and Techniques 58 (8) (2010) 2158–2165. doi:10.1109/TMTT.2010.2053061.

[28] J. Jin, V. V. Liepa, C. Tai, A volume-surface integral equation for electromagnetic scattering by inhomogeneous cylinders, Journal of Electromagnetic Waves and Applications 2 (5/6) (1988) 573–588. doi:10.1163/156939388X00170.

[29] A. Poggio, E. Miller, Integral Equation Solutions of Three-dimensional Scattering Problems, Pergamon, New York, 1973, Ch. 4, pp. 159–264.

[30] Dassault Systèmes, CST Studio Suite 3D EM simulation and analysis software (2020).
URL https://www.3ds.com/products-services/simulia/products/cst-studio-suite/

[31] M. J. Colbrook, L. J. Ayton, A. S. Fokas, The unified transform for mixed boundary condition problems in unbounded domains, Proceedings of the Royal Society A 475 (2222) (2019). doi:10.1098/rspa.2018.0605.

[32] D. G. Crowdy, E. Luca, Solving Wiener–Hopf problems without kernel factorization, Proceedings of the Royal Society A 470 (2170) (2014). doi:10.1098/rspa.2014.0304.

[33] M. J. Colbrook, Extending the unified transform: curvilinear polygons and variable coefficient PDEs, IMA Journal of Numerical Analysis 40 (2) (2020) 976–1004. doi:10.1093/imanum/dry085.